

1 **Microbial strong organic ligand production is tightly coupled to iron in**  
2 **hydrothermal plumes**

3  
4 Colleen L. Hoffman<sup>1,2,3\*†</sup> and Patrick J. Monreal<sup>3,4\*†</sup>, Justine B. Albers<sup>5</sup>, Alastair J.M. Lough<sup>6</sup>, Alyson E.  
5 Santoro<sup>5</sup>, Travis Mellett<sup>3,7</sup>, Kristen N. Buck<sup>7,8</sup>, Alessandro Tagliabue<sup>9</sup>, Maeve C. Lohan<sup>6</sup>, Joseph A.  
6 Resing<sup>1,2,3</sup>, Randelle M. Bundy<sup>3</sup>

7  
8 <sup>1</sup>Joint Institute for the Study of Atmosphere and Ocean, University of Washington, 3737 Brooklyn  
9 Avenue NE, Seattle, WA 98195, USA

10 <sup>2</sup>Cooperative Institute for Climate, Ocean, and Ecosystem Studies, University of Washington,  
11 3737 Brooklyn Avenue NE, Seattle, WA 98195, USA

12 <sup>3</sup>School of Oceanography, University of Washington, 1501 NE Boat Street, Seattle, WA 98195,  
13 USA

14 <sup>4</sup>Earth Systems Program, Stanford University, 473 Via Ortega, Stanford, CA 94305,  
15 USA

16 <sup>5</sup>Department of Ecology, Evolution, and Marine Biology, University of California, Santa Barbara,  
17 CA 93106, USA

18 <sup>6</sup>Department of Ocean and Earth Sciences, National Oceanography Centre, University of  
19 Southampton, European Way, Southampton SO14 3ZH, United Kingdom

20 <sup>7</sup>College of Marine Science, University of South Florida, 140 7<sup>th</sup> Avenue South, St. Petersburg,  
21 FL, 33701, USA

22 <sup>8</sup>College of Earth, Oceans, and Atmospheric Sciences, Oregon State University, 2651 SW Orchard Ave,  
23 Corvallis, OR, 97331, USA

24 <sup>9</sup>Department of Earth, Ocean, and Ecological Sciences, University of Liverpool, 4 Brownlow  
25 Street, Liverpool L69 3GP, United Kingdom

26  
27 †These authors contributed equally and are co-first authors

28 \*Correspondence: Colleen L. Hoffman and Patrick J. Monreal

29 **Email:** [clhoffma@gmail.com](mailto:clhoffma@gmail.com), [pmonreal@uw.edu](mailto:pmonreal@uw.edu)

30

31

32

33

34 **Abstract.** Hydrothermal vents have emerged as important sources of iron to seawater, yet only a subset of  
35 this iron is soluble and persists long enough to impact the deep ocean iron inventory. The longevity and  
36 solubility of iron in seawater is in part governed by strong organic ligands, ~~like siderophores,~~ that are  
37 produced by microorganisms and are a part of the ocean's dissolved organic iron-binding ligand pool.  
38 ~~Organic ligands have long been recognized to support elevated dissolved iron in hydrothermal vent plumes.~~  
39 ~~Siderophores are one group of microbially-produced organic ligands that have especially high binding~~  
40 ~~affinities for iron. Here we present the first direct measurements of siderophore concentrations in~~  
41 ~~hydrothermal vents, which we compare to bulk strong iron-binding ligand concentrations, along these~~  
42 ~~ligands have been hypothesized to aid in the persistence of dissolved iron in hydrothermal environments. To~~  
43 ~~explore this hypothesis, we measured iron and iron-binding ligands including siderophores from 11~~  
44 ~~geochemically distinct sites along a 1,700 km section of the Mid-Atlantic Ridge.~~ Siderophores were found  
45 in hydrothermal plumes at all sites, with proximity to the vent playing an important role in dictating  
46 siderophore type and diversity. The notable presence of amphiphilic siderophores may point to microbial  
47 utilization of siderophores to access particulate hydrothermal iron, and the exchange of dissolved and  
48 particulate iron. The tight coupling between strong ligands and dissolved iron within neutrally buoyant  
49 plumes across distinct hydrothermal environments, and the presence of dissolved siderophores with  
50 siderophore-producing microbial genera, suggests that biological production of ligands influences iron  
51 chemistry in hydrothermal systems.

## 52 1. Introduction

53 Over the last few decades, observations and modelling efforts have increased our understanding about the  
54 critical role organic ligands play in the cycling, transport, and utilization of trace metals (Tagliabue et al.,  
55 2017; Buck et al., 2018; Bundy et al., 2018; Moore et al., 2021; Hawkes et al., 2013b; Kleint et al., 2016).  
56 Iron (Fe) binding organic ligands in seawater have a wide range of sources, which are only just beginning to  
57 be understood. Recent observations suggest that microbial production of siderophores, humic-like substances  
58 and exopolysaccharides are some of the major contributors of marine organic ligands (Hassler et al., 2017),  
59 and microbial production and alteration of ligands influences Fe cycling in environments ranging from  
60 hydrothermal plumes (Cowen and Bruland, 1985; Cowen et al., 1990) to the open ocean (Lauderdale et al.,  
61 2020; Whitby et al., 2024, 2020; Misumi et al., 2013). Strong Fe-binding organic ligands (defined as L<sub>1</sub>  
62 ligands) are a heterogeneous mixture of microbially produced compounds that are operationally classified  
63 based on their binding strength with Fe (defined as  $\log K_{Fe^2, FeL}^{cond} > 12$ ). They are thermodynamically favored  
64 to complex and stabilize external sources of Fe to prevent its scavenging and removal (Fishwick et al., 2014;  
65 Aguilar-Islas et al., 2010).

66  
67 Siderophores are the strongest known Fe-binding organic ligands. They are produced by bacteria and fungi  
68 to facilitate Fe uptake and solubilize otherwise inaccessible phases in the marine environment (Butler, 2005;

Formatted: Font: (Default) Times New Roman, 10 pt

Formatted: Font: 10 pt

Formatted: Font: (Default) Times New Roman, 10 pt

Formatted: Font: 10 pt

Formatted: Font: (Default) Times New Roman, 10 pt

Formatted: Font: (Default) Times New Roman, 10 pt

Formatted: Font: (Default) Times New Roman, 10 pt

Formatted: Font: (Default) Times New Roman, 10 pt

Formatted: Font: (Default) Times New Roman, 10 pt

Formatted: Font: (Default) Times New Roman, 10 pt

Formatted: Font: (Default) Times New Roman, 10 pt

Formatted: Font: (Default) Times New Roman, 10 pt

Formatted: Font: (Default) Times New Roman, 10 pt

Formatted: Font: (Default) Times New Roman, 10 pt

69 Manck et al., 2022). They have primarily been considered an important microbial strategy for Fe acquisition  
70 in the low dissolved Fe (dFe) surface ocean (Vraspir and Butler, 2009; Butler, 2005). However, siderophore  
71 uptake and biosynthesis genes were observed in >70% of Fe-related bacterial transcripts in a hydrothermal  
72 environment in Guaymas Basin (Li et al., 2014), have been identified in oxygen-deficient zones (Moore et  
73 al., 2021), and are a common Fe acquisition strategy within terrestrial and pathogenic ecosystems (Sandy and  
74 Butler, 2009), all of which are environments where Fe concentrations are orders of magnitude higher than  
75 surface seawater.

76  
77 Previous studies have examined ~~unknown total concentrations of~~ Fe-binding ligands in hydrothermal plumes  
78 and throughout the deep ocean (Sander and Koschinsky, 2011; Hawkes et al., 2013b; Mahieu et al., 2024;  
79 Buck et al., 2018; Kleint et al., 2016), as well as siderophores observed below the euphotic zone (Park et al.,  
80 2023; Boiteau et al., 2019; Bundy et al., 2018; Moore et al., 2021). ~~However, no previous studies have ever~~  
81 ~~directly measured siderophores in hydrothermal systems due to the high sample volume requirements,~~  
82 ~~difficulty in obtaining deep ocean trace metal samples, and the time-intensive nature of the analyses.~~ A  
83 'stabilizing agent' (~~i.e. ligands~~) has been proposed for the long-range transport of hydrothermal dFe into the  
84 ocean interior, ~~which has been hypothesized to be inorganic colloids~~ (Fitzsimmons et al., 2017; Fitzsimmons  
85 and Boyle, 2014; Yücel et al., 2011; Lough et al., 2019), ~~or organic ligands including strong ligands and~~  
86 ~~weaker ligands~~ (Hawkes et al., 2013b; Mahieu et al., 2024; Kleint et al., 2016; Hassler et al., 2020; Slagter  
87 et al., 2019), ~~or a combination of the two~~. The role of strong Fe-binding ligands in hydrothermal dFe transport  
88 represents an important knowledge gap in how hydrothermal vents may impact the ocean dFe inventory  
89 (Resing et al., 2015) and how siderophores may influence Fe transformations in hydrothermal  
90 ~~plumes systems~~. ~~While genetic evidence suggests that siderophore cycling may occur in hydrothermal~~  
91 ~~systems~~ (Li et al., 2014), ~~however, no previous studies have ever directly measured siderophores in~~  
92 ~~hydrothermal systems due to the high sample volume requirements, difficulty in obtaining deep ocean trace~~  
93 ~~metal samples, and the time-intensive nature of the analyses.~~ Here, for the first time, we identified  
94 siderophores and siderophore-producing microbes in 11 geochemically distinct hydrothermal ~~plume~~  
95 environments along the slow-spreading (20-50 mm/yr) Mid-Atlantic Ridge (MAR). Four black smokers  
96 (high temperature, high Fe), four off-axis sites, one diffuse vent (low temperature, low Fe), one alkaline vent  
97 (pH 9-11, very low Fe), and one non-vent fracture zone were investigated using both competitive ligand  
98 exchange-adsorptive cathodic stripping voltammetry and state-of-the-art liquid chromatography coupled to  
99 electrospray ionization mass spectroscopy (Boiteau et al., 2016) in a targeted approach to search for known  
100 siderophores and possible compounds present in the L<sub>1</sub> ligand pool in hydrothermal ~~plumes environments~~.  
101 Microbial community analysis was also compared at three sites to understand whether ~~microbial~~  
102 ~~ligands siderophore~~ production impacts Fe transformation in hydrothermal ~~systems plumes~~. Overall, our results  
103 ~~show microbially produced siderophores were present in all sites, and that strong L<sub>1</sub> ligands were tightly~~  
104 ~~coupled to hydrothermal dFe concentrations in neutrally buoyant plume samples in this system. The presence~~

105 of organic ligands produced by bacteria in hydrothermal systems suggest that they play an important role in  
106 deep ocean Fe cycling.

## 107 2. Results and Discussion

### 108 2.1 The role of iron-binding ligands in hydrothermal plumes

109 Strong Fe-binding ligands ( $L_1$ ) have previously been found in neutrally-buoyant hydrothermal plumes across  
110 a variety of systems (Wang et al., 2022; Bennett et al., 2008; Tagliabue et al., 2017; Hawkes et al., 2013b;  
111 Resing et al., 2015; Buck et al., 2018). However, the relationship between organic ligands and dFe have never  
112 been investigated together systematically across a wide variety of vents in the same study. In this work, the  
113 average binding strength and concentration of organic Fe-binding ligands were quantified in 11 vent systems  
114 that spanned a wide range in dFe concentrations (0.41-90 nM) and underlying vent geology. Over 99% of  
115 dFe in the neutrally buoyant plume samples were complexed by  $L_1$  ligands and the ligands were almost  
116 always completely saturated with dFe, meaning Fe-free ‘excess’  $L_1$  ligands capable of binding additional Fe  
117 were present in low concentrations (< 1 nM; **Fig. S1**). As a result, dFe concentrations were tightly coupled  
118 to  $L_1$  ligands in a nearly 1:1 ratio (**Fig. 1d**), similar to previous studies in other neutrally buoyant plumes  
119 (**Fig. 1e**) (Buck et al., 2015, 2018).

120  
121 The strong coupling between dFe and ligands was only observed at sites where  $L_1$  ligands were detected.  
122 Some samples, that were closer to the buoyant plume and vent source, contained high concentrations of  
123 weaker ligands ( $\log K_{Fe,FeL}^{cond} < 12$ , **Table S2-S3**) whose concentrations had no correlation with dFe. This is  
124 consistent with these environments likely being dominated by complex Fe phases, which could include  
125 various inorganic forms (e.g. nanopyrite, Fe-oxyhydroxide) as well as mixed organic phases of Fe as  
126 hydrothermal fluids initially mix with oxygenated seawater. High concentrations of weaker ligands have also  
127 been observed in samples near the vent orifice in previous studies (Hawkes et al., 2013). These ligands can  
128 include humic-like substances, exopolysaccharides, or other organic degradation products. (Slagter et al.,  
129 2019; Hassler et al., 2020; Mahieu et al., 2024; Hawkes et al., 2013b). In this study, we ~~are~~ were not able to  
130 discern the exact chemical composition of the ligands we detect via voltammetric methods, and thus the  
131 weaker and some portion of the stronger ligands we observe likely represent a mix of different inorganic and  
132 organic ligands. Similar to what was described in Hawkes et al. (2013b), the ligands we measure could  
133 represent multiple layers of coordination bonds, forming complex Fe phases, similar to the “onion” concept  
134 (Mackey and Zirino, 1994). For example, colloidal Fe phases are common in hydrothermal vents plumes and  
135 can form aggregates that bind Fe, but not in traditional organic coordination bonds (Fitzsimmons et al., 2017;  
136 Honeyman and Santschi, 1989). There are also likely processes occurring near the vent source in such a  
137 complex environment that cause some Fe phases to be in various stages of disequilibria that we also measure  
138 as ligands via our voltammetric methods.

139

140 The sources of weaker Fe-binding ligands ( $\log K_{Fe,FeL}^{cond} < 12$ ) that have been observed in other hydrothermal  
141 ~~systems/plumes~~ is not well understood, and their impact on Fe cycling over the lifetime of neutrally-buoyant  
142 plume is unclear. Recent studies have shown microbes may use siderophores or siderophore-like (strong  
143 binding ligands) ligands to access Fe associated with weaker ligands — such as humic substances and thiols  
144 — to enhance the bioavailability of Fe (Kuhn et al., 2014; Muller, 2018). However, to date, the few studies  
145 that have explored ligand concentrations and binding strengths within hydrothermal ~~plumes/systems~~ (Buck et  
146 al., 2015; Hawkes et al., 2013c; Buck et al., 2018; Kleint et al., 2016; Sander and Koschinsky, 2011; Mahieu  
147 et al., 2024) have mixed hypotheses as to the role and sources of weaker-type ligands within plumes.  
148 Additional studies are needed to investigate the sources and mechanisms of weaker-type ligands in  
149 hydrothermal plumes and understand their impact on the Fe cycle in hydrothermal ~~systems/plumes~~.

150

151 In the neutrally buoyant plume samples, stronger L<sub>1</sub> ligands were present and were correlated with the dFe  
152 concentrations (Fig. 1) and weaker ligands were no longer dominant. In other systems with a high dFe and  
153 ligand endmember such as estuaries, a decrease in weaker ligands along with dFe concentrations has also  
154 been observed (Buck et al., 2007; Bundy et al., 2014). This has been interpreted as a scavenging of weaker  
155 Fe-ligand complexes, while the dFe that remains in solution is that which is bound to stronger ligands (Bundy  
156 et al., 2014). A similar control on dFe concentrations by L<sub>1</sub> ligands has also been previously observed in  
157 aerosol solubility experiments (Fishwick et al., 2014). There are a few possible explanations for the  
158 correlation of dFe and L<sub>1</sub> ligands in the neutrally-buoyant plume. One possible explanation is that both the  
159 dFe and L<sub>1</sub> ligands originate from the vent fluids themselves, yielding a tightly coupled hydrothermal  
160 endmember. However, the concentration of L<sub>1</sub> ligands did not correlate with excess mantle Helium-3 (<sup>3</sup>He<sub>xs</sub>,  
161 Fig S2, Table S2-S3) (Lough et al., 2022), a nearly conservative tracer of the mixing of hydrothermal fluids  
162 with seawater (Buck et al., 2018). Moreover, our samples closer to the vent source were dominated by weaker  
163 organic ligands showing no correlation to dFe. This suggests the L<sub>1</sub> ligands were not directly sourced from  
164 the vent fluids along with dFe. Biological sources represent another likely explanation for the coupling of L<sub>1</sub>  
165 ligands and dFe, if the ligands observed in the neutrally-buoyant plume are from bacteria that produced them  
166 in surrounding deep ocean seawater that was then entrained, local production from vent-biota and/or  
167 microbial mats, diffusion from microbial production in sediments, or *in-situ* production by bacteria within  
168 the neutrally buoyant plume (Dick et al., 2013; Li et al., 2014; Sheik et al., 2015; Mellett et al., *submitted*).

## 169 2.2 The presence of siderophores in hydrothermal systems

170 Siderophores were measured in a subset of the samples to further explore the source of the L<sub>1</sub> ligands coupled  
171 to dFe in the neutrally-buoyant plume. Marine organic ligand composition changes with environmental  
172 gradients (Gledhill and Buck, 2012; Boiteau et al., 2016), making the structure and functional groups of  
173 siderophores identified in hydrothermal samples of particular interest. Somewhat surprisingly, siderophores  
174 were found in all samples and we observed a large diversity of siderophores with high confidence using mass-  
175 to-charge ratio (*m/z*), MS/MS spectra, and specific chromatographic characteristics (Fig. 2a). On-axis

176 spreading centers contained the highest dFe concentrations (> 20 nM) and wider variety of siderophores than  
177 samples from fracture zones, diffuse, and off-axis sites (dFe ≤ 1 nM). The greatest number of distinct  
178 siderophores were identified at Lucky Strike, Broken Spur, Rainbow, and TAG (Fig. 2). On average, 13  
179 compounds were identified with high confidence per on-axis spreading center sample, compared with 5 per  
180 diffuse/fracture zone sample, and 2.5 per off-axis sample (Fig. 2b, Fig. S4). Mixed-type siderophores —  
181 containing different moieties that bind to Fe(III) — were common at all sites. Hydroxamates were identified  
182 at and around spreading centers, yet none of these were detected with high confidence in samples from  
183 diffuse/fracture zones (Fig. S4). Summed siderophore abundance in neutrally-buoyant plumes above  
184 spreading centers was similarly more than twice that of samples from fracture zones or off-axis (Fig. 2c).  
185 Thus, vent type and proximity played a role in the diversity and abundance of siderophore types observed,  
186 likely related to the diversity of the microbial community and/or unique Fe acquisition strategies across sites.

187

188 Siderophores are putatively part of the operational L<sub>1</sub> ligand pool based on their binding strength (Gledhill  
189 and Buck, 2012), and patterns in their distributions were similar to those of the strong ligands. The peak areas  
190 of each putative siderophore we identified were used as a proxy for concentrations (section 3.3), and these  
191 concentrations significantly correlated with dFe, as observed with dFe and L<sub>1</sub> ligands (Fig. 2b). Siderophores  
192 were present in concentrations similar to the surface ocean (Park et al., 2022; Boiteau et al., 2016; Moore et  
193 al., 2021; Bundy et al., 2018) and were equivalent to concentrations representing 0.01-0.4% of the total L<sub>1</sub>  
194 ligands (Table 1). This is a substantial underestimate of siderophore contributions to the L<sub>1</sub> ligand pool due  
195 to analytical constraints in identifying unknown siderophores. Recent work on siderophore biosynthesis  
196 pathways and advances in genome mining suggest that known siderophores represent a small fraction of what  
197 is expected to be produced in nature (Hider and Kong, 2010; Reitz et al., 2022), and our analyses in this study  
198 were limited to only known siderophores. We also restricted our reporting to compounds identified with very  
199 high confidence (Fig 2a, S3). In addition, most siderophores are not commercially available to use as  
200 standards, and individual siderophores have different ionization or extraction efficiencies. The extraction  
201 efficiency for the solid phase extraction technique is approximately 5-10% for bulk Fe-binding organics  
202 (Bundy et al., 2018) and 40% for a siderophore standard (Waska et al., 2015). Employing both corrections  
203 yields siderophore contributions to the total L<sub>1</sub> pool of 0.1-4% and 0.025-1%, respectively. We are inevitably  
204 missing many naturally occurring unknown compounds, and thus we consider this a lower bound. Regardless  
205 of the small percentage contribution to total L<sub>1</sub> ligands, it is evident that microbially produced siderophores  
206 were ubiquitous across all vent sites and had similar distributional patterns as L<sub>1</sub> ligands. There are also likely  
207 other compounds such as some strong binding humics that are also contributing to the L<sub>1</sub> ligand pool (La glera  
208 and van den Berg, 2009). Future work with much larger water volumes will be able to reduce uncertainty and  
209 identify a greater number of compounds. Still, the identification of siderophores here — and their relationship  
210 with dFe — provides compelling evidence that microbial production of ligands is responsible for at least  
211 some portion of the tight coupling between L<sub>1</sub> and dFe in hydrothermal systems along the MAR.

212

213 The presence and diversity of siderophores identified in this system was surprising given the relatively high  
214 Fe concentrations of hydrothermal environments, but some compelling patterns were observed. Amphiphilic  
215 siderophores comprised 57% of the siderophores in our samples (Fig. S5), supporting the ubiquity of  
216 amphiphilic siderophores in marine environments (Butler and Theisen, 2010). Amphiphilic siderophores  
217 were found in concentrations between 0.3-4.7 pM, with the highest concentrations found at Rainbow (Fig.  
218 2d, Table S6). These concentrations were similar to those observed in the upper ocean (Boiteau et al., 2019,  
219 2016; Bundy et al., 2018). Amphiphilic siderophores have long hydrocarbon tails that can be embedded into  
220 the lipid bilayer of the bacterial cell membrane providing a mechanism to shuttle Fe into the cell and prevent  
221 diffusive loss (Martinez et al., 2003). For example, previous work has shown that low Fe surface waters have  
222 higher concentrations of amphiphilic siderophores compared to high Fe coastal waters (Boiteau et al., 2016),  
223 and amphiphilic siderophores are less common in terrestrial environments (Hider and Kong, 2010).  
224 Amphiphilic siderophores have long hydrocarbon tails that can be embedded into the lipid bilayer of the  
225 bacterial cell membrane providing a mechanism to shuttle Fe into the cell and prevent diffusive loss (Martinez  
226 et al., 2003). Amphiphilic siderophores comprised 57% of the siderophores in our samples (Fig. S5),  
227 supporting the ubiquity of amphiphilic siderophores in marine environments (Butler and Theisen, 2010).  
228 Amphiphilic siderophores were found in concentrations between 0.3-4.7 pM, with the highest concentrations  
229 found at Rainbow (Fig. 2d, Table S6). These concentrations were similar to those observed in the upper  
230 ocean (Boiteau et al., 2019, 2016; Bundy et al., 2018). Marine bacteria produce suites of amphiphilic  
231 siderophores as a way to adapt to the change in hydrophilicity in the surrounding environment (Homann et  
232 al., 2009; Sandy and Butler, 2009). Amphiphilic siderophores in plumes could be a way for bacteria to access  
233 Fe as they are physically transported and cope with strong chemical gradients, similar to the production of  
234 multiple siderophores in terrestrial and pathogenic systems as a means to access inorganic particulate Fe  
235 for cellular uptake and storage (Hider and Kong, 2010).

236

### 237 **2.3 Microbial sources of siderophores in hydrothermal plumes**

238 The high diversity of siderophores across a huge range of hydrothermal vent systems revealed several  
239 surprising aspects of Fe cycling. The biosynthesis of a siderophore is energy-intensive and is regulated by Fe  
240 concentration in the surrounding environment (Rizzi et al., 2019). Siderophore presence suggests that bacteria  
241 are producing these compounds despite the overall higher Fe concentrations in the deep ocean and within  
242 hydrothermal plumes. Consistent with siderophore utilization in terrestrial ecosystems (Hider and Kong,  
243 2010; Sandy and Butler, 2009), one hypothesis is that siderophore production is beneficial to bacteria in the  
244 plumes for transforming Fe from otherwise inaccessible forms, such as particulate nanopyrites or Fe  
245 oxyhydroxides that are present close to the vent source. To explore the potential for microbial production of  
246 siderophores, we examined microbial community composition around Rainbow (St. 11, 17) and Lucky Strike  
247 (St. 7; **Table 1, Table S1**) using 16S rRNA gene-based amplicon sequencing to detect bacteria with the  
248 metabolic potential to synthesize siderophores (**Fig. 3, S11**). The, where the presence of taxa encoding

249 siderophore biosynthetic gene clusters indicates whether the microbial community ~~has the~~ genetically  
250 ~~potential~~ capable of producing the compounds we observed. Bacterial genera containing known siderophore-  
251 producers were found at all three MAR sites examined, and putative siderophore-producers represented 3-  
252 20% of the relative abundance of the community (Fig. 3). Putative siderophore-producers were more  
253 abundant in the 3  $\mu\text{m}$  (particle-attached) size fraction than in the 0.2  $\mu\text{m}$  (free-living) fraction, suggesting  
254 siderophore production is more common in particle-associated bacteria in hydrothermal environments.  
255

256 We found microbial genera in our samples that can produce a subset of the siderophores identified here,  
257 including ferrioxamines, vibrioferrin, and acinetoferrin (Vraspir and Butler, 2009; Butler, 2005; Moore et al.,  
258 2021; Bundy et al., 2018; Boiteau et al., 2016). Genera with the genetic potential to produce ferrioxamines  
259 were present at all three sites, while those known to produce vibrioferrin were present at Lucky Strike and  
260 Rainbow, and those producing acinetoferrin were also present at Rainbow (Table S1, S7). Mycobactins were  
261 detected with high confidence in every sample of this study, and genes encoding mycobactin have been  
262 detected in a cultured organism from a hydrothermal system (Gu et al., 2019), but no mycobactin producers  
263 were identified in this study. We detected woodybactin D with high confidence in 5 out of 11 sites analysed  
264 and compared to the known siderophore library (Fig. 2). Woodybactin D Although these biosynthetic genes  
265 were not identified in any of the genera from the 16S rRNA gene amplicon sequences observed; however,  
266 woodybactin D is a carboxylate siderophore isolated from *Shewanella* (Carmichael et al., 2019), and groups  
267 of deep-sea *Shewanella* (Kato and Nogi, 2001) were found in the dataset (Fig. S11). The biosynthesis genes  
268 for many of the siderophores identified are unknown. Thus, finding genera capable of producing only a subset  
269 of the siderophores characterized is not surprising. The observation that a significant portion of the *in-situ*  
270 microbial community is capable of synthesizing siderophores (Fig. 3) suggests that siderophore production  
271 is more widespread in the deep ocean than previously believed and could contribute to the “microbial iron  
272 pump” in hydrothermal plumes (Li et al., 2014).  
273

#### 274 2.4 The impact of strong ligands and siderophores on dissolved iron in neutrally-buoyant plumes

275 Evidence that siderophores are ubiquitous in the marine environment — including higher Fe environments  
276 — has been increasing (Park et al., 2022). The high dFe associated with hydrothermal plumes may still not  
277 be high enough to suppress siderophore production due to the elevated Fe requirements of heterotrophic  
278 bacteria (Tortell et al., 1996). It is also likely that not all of the Fe is bio-accessible in hydrothermal plumes.  
279 Soil microbes secrete siderophores to solubilize particulate Fe (Crowley et al., 1991) and similar processes  
280 could be occurring in hydrothermal plumes, where Fe mineral phases associated with organic compounds are  
281 common (Hoffman et al., 2020; Toner et al., 2009; Hoffman et al., 2018; German and Seyfried, 2014; Holden  
282 et al., 2012; Fitzsimmons et al., 2017). Although our measurements suggest that dFe in the neutrally-buoyant  
283 plume is likely dominated by organic complexation, the  $L_1$  measurements alone cannot distinguish between  
284 purely organic phases or a mixture of inorganic and organic ligands in complex aggregations or small  
285 colloids, as discussed above (section 2.1). Given the evidence from particulate Fe studies in neutrally-buoyant



286 plumes (Yücel et al., 2011; Fitzsimmons et al., 2014; Hoffman et al., 2020; Toner et al., 2009; Fitzsimmons  
287 et al., 2017; Hoffman et al., 2018), it is highly likely that some portion of what is detected in the L<sub>1</sub> pool is a  
288 mixture of organic and inorganic Fe in small colloids which are operationally in the dFe pool (Fitzsimmons  
289 et al., 2017). It is also telling that ~~4-5x more most~~ siderophore-producing genera were found to be particle-  
290 associated (Fig. 3), providing additional evidence that siderophores might be produced to solubilize  
291 particulate Fe or access other colloidal phases. Further work that assesses why bacteria are producing  
292 siderophores in neutrally buoyant plumes will be important for understanding microbial metabolism in these  
293 systems, and the impact of siderophore production on Fe dispersal.

294

295 Organic Fe-binding ligands have been implicated in playing a critical role in the preservation and transport  
296 of hydrothermal dFe into the ocean interior (Bennett et al., 2011; Hoffman et al., 2018; Fitzsimmons et al.,  
297 2017; Toner et al., 2009; Bennett et al., 2008; Resing et al., 2015; Buck et al., 2018; Sander and Koschinsky,  
298 2011). In this work, L<sub>1</sub> ligands were tightly coupled to dFe in neutrally buoyant plumes along the MAR and  
299 the presence of siderophores in these samples provided evidence for the first time, that at least some of these  
300 ligands are microbially produced. How these complexes may facilitate the exchange of Fe between dissolved  
301 and particulate phases (Fitzsimmons et al., 2017), and whether siderophores are present across additional  
302 hydrothermal vent systems will aid in ~~constraining understanding how microorganisms might play a role, the~~  
303 ~~biogeochemical levels of their shaping the importance of microbial feedbacks in impacting the~~ hydrothermal  
304 dFe supply to the deep ocean.

305

### 306 **3. Appendix: Materials and Methods**

#### 307 **3.1 Sampling and cruise transect**

308 Samples were collected as part of the 2017-2018 U.K. GEOTRACES GA13 section cruise along the Mid-  
309 Atlantic Ridge (FRidge GA13). Water samples from 11 venting and near venting locations were collected  
310 using a Seabird 911 conductivity, temperature, and depth (CTD) titanium rosette using conducting Kevlar  
311 wire with an oxidation-reduction potential (ORP) sensor to detect plumes. Teflon coated OTE (Ocean Test  
312 Equipment) bottles were pressurized to approximately 7 psi with 0.2 µm filtered air using an oil free  
313 compressor. A Sartobran 300 (Sartorius) filter capsule (0.2 µm) was used to collect filtered seawater samples  
314 into clean 250 mL LDPE sample bottles. Bottles and caps were rinsed 3 times with the filtered sample before  
315 being filled. Samples were stored frozen at -20°C for Fe-organic ligand characterization by voltammetry and  
316 mass spectrometry.

#### 317 **3.2 Fe-binding ligand concentration and binding strengths Competitive Ligand Exchange-Adsorptive** 318 **Cathodic Stripping Voltammetry**

319 Fe-binding ligand concentrations and binding strengths (defined as conditional binding constants,  $\log K_{Fe,FeL}^{cond}$   
320 > 12) were determined by competitive ligand exchange-adsorptive cathodic stripping voltammetry (CLE-

321 ACSV) with a BASi controlled growth mercury electrode (CGME) with an Ag/AgCl<sup>-</sup> reference electrode  
322 and platinum auxiliary electrode (Bioanalytical Systems Incorporated). Using previously established  
323 methods (Abualhija and van den Berg, 2014; Buck et al., 2015; Hawkes et al., 2013c; Buck et al., 2018;  
324 Bundy et al., 2018), 40 frozen filtrate (<0.2 μm) samples with dFe concentrations between 0.41-11.67 nM  
325 (**Table S1-S2**) were thawed in a 4°C fridge prior to analysis. A 15-point titration curve was analyzed for each  
326 sample. Briefly, within each titration, every point sequentially received 10 mL of sample, 7.5 mM of borate-  
327 ammonium buffer, 10 μM salicylaldehyde (SA) added ligand, and a dFe addition ([see Supplemental Methods](#)  
328 [1.1. for additional details](#)). Samples were then equilibrated overnight before being measured on the BASi.  
329 Data was collected using the *Epsilon Eclipse Electrochemical Analyzer* (v.213) with a deposition time of 120  
330 seconds and analyzed using *ElectroChemical Data Software* (v2001-2014) and *PromCC* (v2008-2018) to  
331 determine peak areas and Fe-binding ligand parameters, respectively. All results were confirmed to fall  
332 within the analytical window of the method by comparing the side reaction coefficient of the added ligand  
333  $\alpha_{SA}$  to the side reaction coefficient of the natural ligands detected ( $\alpha_L$ ). If the  $\alpha_L$  was within an order of  
334 magnitude of  $\alpha_{SA}$  then the results were deemed to fall within the analytical window.

### 335 **3.3 Reverse Titration-CLE-ACSV**

336 Reverse titration-CLE-ACSV (RT-CLE-ACSV) (Hawkes et al., 2013a) was completed on 10 samples from  
337 Broken Spur, and TAG hydrothermal vent fields with dFe concentrations between 19.01-90.25 nM (**Table**  
338 **S3**). Briefly, a 10-point titration curve was analyzed for each sample with each titration point consisting of  
339 10 mL of sample buffered with 7.5 mM boric acid and the competitive ligand 1-nitroso-2-naphthol (NN)  
340 additions. All samples were analyzed on a BASi Controlled Growth Mercury Electrode (CGME) with the  
341 *Epsilon Eclipse Electrochemical Analyzer* (v.213) and deposition time of 120 seconds. For each sample,  
342 competitive ligand NN additions were 0.5, 1, 2, 3, 4, 6, 9, 15, 20, and 40 μM. Samples were equilibrated  
343 overnight and purged with N<sub>2</sub> (99.99%) for 5 minutes before analysis. At the end of each titration, three Fe  
344 additions (3-15 nM) were added to the final titration point to get the total concentration of Fe in equilibrium  
345 with ligands. Data was analyzed using *ElectroChemical Data Software* (v2001-2014) to acquire peak areas  
346 and a package in R using the model parameters of  $\beta_{FeNN3} = 5.12 \times 10^{16}$ ,  $\chi_{min} = 0.8$ ,  $\chi_{max} = 0.9$ , and  $cI_{high} =$   
347  $0.75$  to determine the Fe-binding ligand parameters (Hawkes et al., 2013a). These parameters were chosen  
348 based on the recommendations for undersaturated samples and titrations curves where  $ip_{max}$  was not reached  
349 (Hawkes et al., 2013a). All other parameters within the model we kept at the default values.

### 350 **3.4 Siderophore quantification and characterization**

351 In addition to measuring Fe-binding ligands by voltammetry, we also identified and quantified siderophores.  
352 Between 0.65-1.5 L of 0.2 μm filtered seawater pooled from ligand samples at each site (described above)  
353 was pumped slowly (15-20 mL min<sup>-1</sup>) onto a polystyrene-divinylbenzene (Bond Elut ENV) solid phase  
354 extraction (SPE) column (Bundy et al., 2018; Boiteau et al., 2016). SPE columns were rinsed with MilliQ  
355 and stored at -20°C until analysis. For the analytical measurements, samples were thawed in the dark, eluted

356 in 12 mL of distilled methanol, and dried down to between 0.2-0.5 mL of sample eluent (**Table S1**). Aliquots  
357 were analyzed by reverse-phase liquid chromatography (LC) on a trace metal clean bio-inert LC (Thermo  
358 Dionex 3000 NCS). The LC was interfaced with an electrospray ionization-mass spectrometer (ESI-MS;  
359 Thermo Q-Exactive HF) to identify and quantify the compounds based on accurate mass ( $MS^1$ ) and the  
360 fragmentation ( $MS^2$ ) data (Bundy et al., 2018; Boiteau et al., 2016). MSconvert (Proteowizard) was used to  
361 convert MS data to an open source mzxML format, and two stages of data processing were conducted using  
362 modified versions of previously reported R scripts (Bundy et al., 2018; Boiteau et al., 2016). In the first stage,  
363 mzxML files were read into R using new package “RaMS” (Kumler and Ingalls, 2022), and extracted ion  
364 chromatograms (EICs) were generated for each targeted  $m/z$  of interest from an in-house database of  
365 siderophores. The  $m/z$  targets were the ionized apo,  $^{54}\text{Fe}$ -bound, and  $^{56}\text{Fe}$ -bound version of each siderophore,  
366 with a tolerance of 7.5 ppm. Putative siderophore candidates were filtered through a series of hard thresholds,  
367 such that  $MS^1$  spectra were quality controlled to contain a minimum of 25 datapoints and the maximum  
368 intensity of each EIC was greater than  $1e4$  counts. Spectra meeting these criteria and containing either  $^{54}\text{Fe}$ -  
369 bound and  $^{56}\text{Fe}$ -bound  $m/z$  peaks within 30 seconds of each other or an apo peak were displayed for the user  
370 to further inspect peak quality and make the final decision of whether to move on to stage two of processing  
371 with a given siderophore candidate.

372

373 Stage two of processing extracted  $MS^2$  spectra of the apo and Fe-bound forms of candidate siderophores to  
374 compare with the predicted  $MS^2$  generated by *in silico* fragmenter MetFrag (Ruttkies et al., 2016). The *in*  
375 *silico* fragmenter feature was run with a tolerance of 10 ppm on “[M+H]<sup>+</sup>” and “[M+Na]<sup>+</sup>” modes. A  
376 confidence level of 1-4, from highest to lowest confidence, was then assigned to putative siderophores based  
377 on the following criteria: (1) peaks were present in  $MS^1$  and  $MS^2$  spectra, and at least one of the three most-  
378 intense  $MS^2$  fragments matched *in silico* fragmentation, (2) peaks were present in  $MS^1$  and  $MS^2$  spectra, and  
379 smaller-intensity fragments matched *in silico* fragmentation, (3) peaks were present in  $MS^1$  and  $MS^2$  spectra,  
380 but little to no fragments matched *in silico* fragmentation, and (4) nicely shaped peaks were identified in  $MS^1$   
381 spectra but no  $MS^2$  spectra was collected (outlined in **Table S5**; example spectra in **Fig. S6-S9**). The  
382 confidence levels were modelled after reporting standards for metabolite identification (Sumner et al., 2007).  
383 MetFrag pulls chemical structures from publicly-available databases like PubChem or COCONUT (Sorokina  
384 et al., 2021), which contain most, but not all variations of siderophores. As such, Fe-bound candidates were  
385 usually run against the apo form available in the database, and for siderophores with similar structures but  
386 variations in fatty chain length or double bond placement, sometimes only one parent structure was available.

387

388 A 5-point standard curve with known concentrations of siderophore ferrioxamine E was used for  
389 quantification of putative siderophores, with a limit of detection of 0.257 nM in the eluent (**Fig. S10**), or  
390 0.07-0.21 pM in the sample depending on sample-to-eluent volume ratio at each site (**Table S1**).  $MS^1$  peaks  
391 were integrated for all putatively identified siderophores and peak areas were converted to concentration  
392 using the standard curve and the concentration factor of sample volume to eluent volume (**Fig. S10**).

393 Commercial standards are not available for most siderophores, and different compounds have distinct  
394 ionization efficiencies in ESI-MS. Thus, the siderophore concentrations reported here are estimates of  
395 siderophore concentrations in these environments based on ferrioxamine E, chosen for its commercial  
396 availability and use in prior studies (e.g., (Boiteau et al., 2016)). Additionally, 1 mM of cyanocobalamin was  
397 added as an internal standard to each sample aliquot to address any changes in sensitivity during LC-ESI-MS  
398 runs. All putative siderophores that were identified with peak areas less than the detection limit were  
399 discarded, and all remaining putative compounds with at least confidence levels 1 and 2 at one site were  
400 included in the manuscript and are referred to as siderophores throughout. Siderophore identifications remain  
401 putative due to inherent uncertainty with assignments by mass, but the confidence levels were designed such  
402 that high confidence candidates contain siderophore-like moieties in their fragments. Limited sample  
403 volumes prevented analysis via LC-ICP-MS like previous studies, which, in addition to greater availability  
404 of commercial standards and more analytical comparisons between ferrioxamine E with other siderophore  
405 types, would allow definitive characterization in future studies. Confidence level 3 and 4 putative  
406 siderophores are only included in the Supplementary Information (Table S6). In a final step of quality  
407 control, EICs for  $^{13}\text{C}$  isotopologues of candidates were inspected to verify matching peak structure.

### 408 3.5 Microbial community analysis

409 Microbial community composition was assessed in neutrally buoyant plumes and near venting sites at three  
410 sites: Lucky Strike (Station 7; 1670 m), 10 km S of Rainbow (Station 17; 2000 m), and 200 km E of Rainbow  
411 (Station 11; 600 m, 1600 m and 2250 m). A range of 1- 2 L of sea water were filtered by pressure filtration  
412 through sequential 25 mm membrane filters housed in polypropylene filter holders (Whatman SwinLok, GE  
413 Healthcare, Pittsburgh, Pennsylvania) using a peristaltic pump and silicone tubing. Samples first passed  
414 through a 3  $\mu\text{m}$  pore-size polyester membrane filter (Sterlitech, Auburn, Washington) then onto a 0.2  $\mu\text{m}$   
415 pore-size polyethersulfone membrane filter (Supor-200, Pall Corporation, Port Washington, New York).  
416 Pump tubing was acid washed with 10% hydrochloric acid and flushed with ultrapure water between each  
417 sample. The filters were flash frozen in liquid nitrogen in 2 mL gasketed bead beating tubes (Fisher Scientific)  
418 at sea.

419  
420 Nucleic acids (DNA) were extracted as described previously (Santoro et al., 2010), with slight modifications.  
421 Briefly, cells on the filters were lysed directly in the bead beating tubes with sucrose-ethylene diamine  
422 tetraacetic acid (EDTA) lysis buffer (0.75 M sucrose, 20 mM EDTA, 400 mM NaCl, 50 mM Tris) and 1%  
423 sodium dodecyl sulfate. Tubes were then agitated in a bead beating machine (Biospec Products) for 1 min,  
424 and subsequently heated for 2 min. at 99°C in a heat block. Proteinase K (New England Biolabs) was added  
425 to a final concentration of 0.5 mg/mL. Filters were incubated at 55°C for approximately 4 h and the resulting  
426 lysates were purified with the DNeasy kit (Qiagen) using a slightly modified protocol (Santoro et al., 2010).  
427 The purified nucleic acids were eluted in 200  $\mu\text{L}$  of DNase, RNase-free water, and quantified using a  
428 fluorometer (Qubit and Quanti-T HS reagent, Invitrogen Molecular Probes).

429

430 The 16S rRNA gene was amplified in all samples using V4 primers (Apprill et al., 2015; Parada et al., 2016)  
431 (515F-Y and 806RB) following a previously established protocol (Stephens et al., 2020). Amplicons were  
432 sequenced using a paired-end 250bp run on an Illumina MiSeq 500 and demultiplexed by the UC Davis  
433 Genome Center. The resulting 16S rRNA amplicon sequences were filtered and trimmed using the DADA2  
434 pipeline in R(Callahan et al., 2016). Taxonomic assignments were made with version 138.1 of the SILVA  
435 SSU database (Quast et al., 2013) (silva\_nr99\_v138.1\_wSpecies\_train\_set.fa.gz ;  
436 doi:10.5281/zenodo.4587955; accessed March 2022). Chloroplast and mitochondrial sequences were filtered  
437 out of the dataset using the 'phyloseq' R package (v 1.38.0), after which samples had read depths ranging  
438 from 9375 – 65486 reads (average  $28425 \pm 20014$  reads) and represented 1010 unique amplicon sequence  
439 variants (ASVs). Read counts were transformed from absolute to relative abundance and taxa were  
440 aggregated to the Family level. The ten most abundant families present in each sample were visualized using  
441 the 'ggplot2' package (v. 3.3.5).

442

443 In order to assess the potential of the observed prokaryotic taxa to produce siderophores, we downloaded all  
444 siderophore biosynthetic gene clusters (BGCs) in the antismash secondary metabolite database ( $n = 7909$ )  
445 and used text-string matching to compare genera containing these BGCs to the genera found in our 16S rRNA  
446 gene dataset(Blin et al., 2021). We cross-referenced the nomenclature of antismash-predicted siderophores  
447 with that of the siderophores identified by LC-ESI-MS in this study, accounting for minor differences in  
448 naming convention between the two databases, to determine if microbial community members present at  
449 each site were predicted to make any of the siderophores that were measured at that site. Station 38 and  
450 Station 12 were the closest sites with siderophore measurements for comparison against the taxonomic  
451 samples taken at 200 km E of Rainbow and 10 km S of Rainbow, respectively. Samples for microbial  
452 taxonomy and siderophore identity were taken from the same location at Lucky Strike and thus directly  
453 compared.

454

#### 455 **Data Availability**

456 The CSV data reported in this study has been deposited at Zenodo under the DOI:  
457 <http://doi.org/10.5281/zenodo.7325154>. The LC-ES-MS data has been deposited on Massive under the DOI:  
458 <http://doi.org/doi.10.25345/C5V97ZW7N>. Microbial 16S rRNA data have been deposited on GenBank under  
459 the accession number BioProject #PRJNA865382. All data is freely available on each of these data  
460 repositories.

461

462

#### 463 **Acknowledgments**

464 We acknowledge the captain and crew of the R/V *James Cook*, Chief Scientist Alessandro Tagliabue, and  
465 Noah Gluschankoff for supporting this work. This study was a part of the FeRidge project (GEOTRACES

466 section GA13) which was supported by the Natural Environment Research Council funding (NERC United  
467 Kingdom Grants NE/N010396/1 to MCL and NE/N009525/1 to AT). The International GEOTRACES  
468 Programme is possible in part thanks to the support from the U.S. National Science Foundation (Grant OCE-  
469 1840868) to the Scientific Committee on Oceanic Research (SCOR). CLH was funded by JISAO/CICOES  
470 postdoctoral fellowship. PJM was funded through the NOAA Hollings Scholar summer program. JR was  
471 funded by NOAA Ocean Exploration and Research, NOAA Earth-Ocean Interactions programs at NOAA-  
472 Pacific Marine Environmental Lab (PMEL #5955), and UW-CICOES (CICOES #2024-1385). Part of this  
473 work was carried out in the University of Washington TraceLab, which receives support from the M.J.  
474 Murdock Charitable Trust in conjunction with the University of Washington College of Environment, and  
475 the Pacific Marine Environmental Labs at the National Oceanic and Atmospheric Administration. Parts of  
476 this work was also carried out in Dr. Anitra Ingalls laboratory with the help of Laura Truxa and Dr. Jiwoon  
477 Park at the University of Washington-School of Oceanography.

478

479 **Author Contributions:** Manuscript preparation, sample/data processing, CSV analysis, and interpretation  
480 LC-ESI-MS data analysis and interpretation (C.L.H. and P.J.M.), microbial analysis and interpretation  
481 (J.B.A. and A.E.S.), dissolved iron and derived excess  $^3\text{He}_{\text{xs}}$  measurements, sample collection (A.J.M. L. and  
482 M.C.L.), microbial data collection and ligand data interpretation (T.M. and K.N.B.), and project design and  
483 planning, data interpretation, and mentoring (A.T., M.C.L., J.A.R., and R.M.B.). All authors were involved  
484 in editing and revision of the manuscript.

485

486 **Competing Interest Statement:** The authors declare no competing interests.

487

## 488 **References**

489 Abualhaja, M. M. and van den Berg, C. M. G.: Chemical speciation of iron in seawater using catalytic  
490 cathodic stripping voltammetry with ligand competition against salicylaldehyde, *Mar. Chem.*, 164, 60–74,  
491 <https://doi.org/10.1016/j.marchem.2014.06.005>, 2014.

492 Aguilar-Islas, A. M., Wu, J., Rember, R., Johansen, A. M., and Shank, L. M.: Dissolution of aerosol-derived  
493 iron in seawater: Leach solution chemistry, aerosol type, and colloidal iron fraction, *Mar. Chem.*, 120, 25–  
494 33, 2010.

495 Apprill, A., McNally, S., Parsons, R., and Weber, L.: Minor revision to V4 region SSU rRNA 806R gene  
496 primer greatly increases detection of SAR11 bacterioplankton, *Aquat. Microb. Ecol.*, 75, 129–137,  
497 <https://doi.org/10.3354/ame01753>, 2015.

498 Bazylev, B. A.: Allochemical Metamorphism of Mantle Peridotites in the Hayes Fracture Zone of the North  
499 Atlantic, *Petrology*, 5, 362–379, 1997.

500 Beaulieu, S. E. and Szafranski, K. M.: InterRidge Global Database of Active Submarine Hydrothermal Vent  
501 Fields Version 3.4, <https://doi.org/10.1594/PANGAEA.917894>, 2020.

502 Bennett, S. a., Achterberg, E. P., Connelly, D. P., Statham, P. J., Fones, G. R., and German, C. R.: The

503 distribution and stabilisation of dissolved Fe in deep-sea hydrothermal plumes, *Earth Planet. Sci. Lett.*, 270,  
504 157–167, <https://doi.org/10.1016/j.epsl.2008.01.048>, 2008.

505 Bennett, S. a., Hansman, R. L., Sessions, A. L., Nakamura, K. ichi, and Edwards, K. J.: Tracing iron-fueled  
506 microbial carbon production within the hydrothermal plume at the Loihi seamount, *Geochim. Cosmochim.*  
507 *Acta*, 75, 5526–5539, <https://doi.org/10.1016/j.gca.2011.06.039>, 2011.

508 Blin, K., Shaw, S., Kautsar, S. A., Medema, M. H., and Weber, T.: The antiSMASH database version 3:  
509 Increased taxonomic coverage and new query features for modular enzymes, *Nucleic Acids Res.*, 49, D639–  
510 D643, <https://doi.org/10.1093/nar/gkaa978>, 2021.

511 Boiteau, R. M., Mende, D. R., Hawco, N. J., McIlvin, M. R., Fitzsimmons, J. N., Saito, M. A., Sedwick, P.  
512 N., DeLong, E. F., and Repeta, D. J.: Siderophore-based microbial adaptations to iron scarcity across the  
513 eastern Pacific Ocean, *Proc. Natl. Acad. Sci.*, 113, 14237–14242, <https://doi.org/10.1073/pnas.1608594113>,  
514 2016.

515 Boiteau, R. M., Till, C. P., Coale, T. H., Fitzsimmons, J. N., Bruland, K. W., and Repeta, D. J.: Patterns of  
516 iron and siderophore distributions across the California Current System, *Limnol. Oceanogr.*, 64, 376–389,  
517 <https://doi.org/10.1002/lno.11046>, 2019.

518 Buck, K. N., Sohst, B., and Sedwick, P. N.: The organic complexation of dissolved iron along the U.S.  
519 GEOTRACES (GA03) North Atlantic Section, Deep. Res. Part II Top. Stud. Oceanogr., 116, 152–165,  
520 <https://doi.org/10.1016/j.dsr2.2014.11.016>, 2015.

521 Buck, K. N., Sedwick, P. N., Sohst, B., and Carlson, C. A.: Organic complexation of iron in the eastern  
522 tropical South Pacific: Results from US GEOTRACES Eastern Pacific Zonal Transect (GEOTRACES cruise  
523 GP16), *Mar. Chem.*, 201, 229–241, <https://doi.org/10.1016/j.marchem.2017.11.007>, 2018.

524 Bundy, R. M., Boiteau, R. M., McLean, C., Turk-Kubo, K. A., McIlvin, M. R., Saito, M. A., Mooy, B. A.  
525 Van, and Repeta, D. J.: Distinct Siderophores Contribute to Iron Cycling in the Mesopelagic at Station  
526 ALOHA, *Front. Mar. Sci.*, 1–15, <https://doi.org/10.3389/fmars.2018.00061>, 2018.

527 Butler, A.: Marine siderophores and microbial iron mobilization., *Biometals*, 18, 369–374,  
528 <https://doi.org/10.1007/s10534-005-3711-0>, 2005.

529 Butler, A. and Theisen, R. M.: Iron(III)-siderophore coordination chemistry: Reactivity of marine  
530 siderophores., *Coord. Chem. Rev.*, 254, 288–296, <https://doi.org/10.1016/j.ccr.2009.09.010>, 2010.

531 Callahan, B. J., McMurdie, P. J., Rosen, M. J., Han, A. W., Johnson, A. J. A., and Holmes, S. P.: DADA2:  
532 High-resolution sample inference from Illumina amplicon data, *Nat. Methods*, 13, 581–583,  
533 <https://doi.org/10.1038/nmeth.3869>, 2016.

534 Carmichael, J. R., Zhou, H., and Butler, A.: A suite of asymmetric citrate siderophores isolated from a marine  
535 *Shewanella* species, *J. Inorg. Biochem.*, 198, 1–6, <https://doi.org/10.1016/j.jinorgbio.2019.110736>, 2019.

536 Cowen, J. P. and Bruland, K. W.: Metal deposits associated with bacteria: implications for Fe and Mn marine  
537 biogeochemistry, *Deep Sea Res. Part A. Oceanogr. Res. Pap.*, 32, 253–272, [https://doi.org/10.1016/0198-  
538 0149\(85\)90078-0](https://doi.org/10.1016/0198-0149(85)90078-0), 1985.

539 Cowen, J. P., Massoth, G. J., and Feely, R. A.: Scavenging rates of dissolved manganese in a hydrothermal  
540 vent plume, *Deep Sea Res. Part A. Oceanogr. Res. Pap.*, 37, 1619–1637, [https://doi.org/10.1016/0198-  
541 0149\(90\)90065-4](https://doi.org/10.1016/0198-0149(90)90065-4), 1990.

542 Crowley, D. E., Wang, Y. C., Reid, C. P. P., and Szanislo, P. J.: Mechanisms of iron acquisition from  
543 siderophores by microorganisms and plants, *Plant Soil*, 130, 179–198, 1991.

544 Dick, G. J., Anantharaman, K., Baker, B. J., Li, M., Reed, D. C., and Sheik, C. S.: The microbiology of deep-  
545 sea hydrothermal vent plumes: Ecological and biogeographic linkages to seafloor and water column habitats,

546 Front. Microbiol., 4, 1–16, <https://doi.org/10.3389/fmicb.2013.00124>, 2013.

547 Fishwick, M. P., Sedwick, P. N., Lohan, M. C., Worsfold, P. J., Buck, K. N., Church, T. M., and Ussher, S.  
548 J.: The impact of changing surface ocean conditions on the dissolution of aerosol iron, *Global Biogeochem.*  
549 *Cycles*, 28, 1235–1250, <https://doi.org/10.1002/2014GB004921>, 2014.

550 Fitzsimmons, J. N. and Boyle, E. A.: Assessment and comparison of Anopore and cross flow filtration  
551 methods for the determination of dissolved iron size fractionation into soluble and colloidal phases in  
552 sea water, *Limnol. Oceanogr. Methods*, 12, 246–263, <https://doi.org/10.4319/lom.2014.12.246>, 2014.

553 Fitzsimmons, J. N., Boyle, E. a., and Jenkins, W. J.: Distal transport of dissolved hydrothermal iron in the  
554 deep South Pacific Ocean, *Proc. Natl. Acad. Sci.*, 111, 16654–16661,  
555 <https://doi.org/10.1073/pnas.1418778111>, 2014.

556 Fitzsimmons, J. N., John, S. G., Marsay, C. M., Hoffman, C. L., Nicholas, S. L., Toner, B. M., German, C.  
557 R., and Sherrell, R. M.: Iron persistence in the distal hydrothermal plume supported by dissolved – particulate  
558 exchange, *Nat. Geosci.*, 10, 1–8, <https://doi.org/10.1038/ngeo2900>, 2017.

559 German, C. and Seyfried, W. E.: *Hydrothermal Processes*, 2nd ed., Elsevier Ltd., 1–39 pp.,  
560 <https://doi.org/10.1016/B978-0-08-095975-7.00201-1>, 2014.

561 Gledhill, M. and Buck, K. N.: The organic complexation of iron in the marine environment: A review, *Front.*  
562 *Microbiol.*, 3, 1–17, <https://doi.org/10.3389/fmicb.2012.00069>, 2012.

563 Gu, H., Sun, Q., Luo, J., Zhang, J., and Sun, L.: A First Study of the Virulence Potential of a *Bacillus subtilis*  
564 Isolate From Deep-Sea Hydrothermal Vent, *Front. Cell. Infect. Microbiol.*, 9, 1–14,  
565 <https://doi.org/10.3389/fcimb.2019.00183>, 2019.

566 Hassler, C., Cabanes, D., Blanco-ameijeiras, S., Sander, S. G., and Benner, R.: Importance of refractory  
567 ligands and their photodegradation for iron oceanic inventories and cycling, *Mar. Freshw. Res.*, 71, 311–320,  
568 2020.

569 Hassler, C. S., van den Berg, C. M. G., and Boyd, P. W.: Toward a regional classification to provide a more  
570 inclusive examination of the ocean biogeochemistry of iron-binding ligands, *Front. Mar. Sci.*, 4,  
571 <https://doi.org/10.3389/fmars.2017.00019>, 2017.

572 Hawkes, J. A., Gledhill, M., Connelly, D. P., and Achterberg, E. P.: Characterisation of iron binding ligands  
573 in seawater by reverse titration, *Anal. Chim. Acta*, 766, 53–60, <https://doi.org/10.1016/j.aca.2012.12.048>,  
574 2013a.

575 Hawkes, J. A., Connelly, D. P., Gledhill, M., and Achterberg, E. P.: The stabilisation and transportation of  
576 dissolved iron from high temperature hydrothermal vent systems, *Earth Planet. Sci. Lett.*, 375, 280–290,  
577 <https://doi.org/10.1016/j.epsl.2013.05.047>, 2013b.

578 Hawkes, J. A., Connelly, D. P., Gledhill, M., and Achterberg, E. P.: The stabilisation and transportation of  
579 dissolved iron from high temperature hydrothermal vent systems, *Earth Planet. Sci. Lett.*, 375, 280–290,  
580 <https://doi.org/10.1016/j.epsl.2013.05.047>, 2013c.

581 Hider, R. C. and Kong, X.: Chemistry and biology of siderophores, *Nat. Prod. Rep.*, 27, 637–657,  
582 <https://doi.org/10.1039/b906679a>, 2010.

583 Hoffman, C. L., Nicholas, S. L., Ohnemus, D. C., Fitzsimmons, J. N., Sherrell, R. M., German, C. R., Heller,  
584 M. I., Lee, J. mi, Lam, P. J., and Toner, B. M.: Near-field iron and carbon chemistry of non-buoyant  
585 hydrothermal plume particles, Southern East Pacific Rise 15°S, *Mar. Chem.*, 201, 183–197,  
586 <https://doi.org/10.1016/j.marchem.2018.01.011>, 2018.

587 Hoffman, C. L., Schladweiler, C., Seaton, N. C. A., Nicholas, S. L., Fitzsimmons, J., Sherrell, R. M., German,  
588 C. R., Lam, P., and Toner, B. M.: Diagnostic morphology and solid-state chemical speciation of



589 hydrothermally derived particulate Fe in a long-range dispersing plume, *ACS Earth Sp. Chem.*, 4, 1831–  
590 1842, <https://doi.org/10.1021/acsearthspacechem.0c00067>, 2020.

591 Holden, J., Breier, J., Rogers, K., Schulte, M., and Toner, B.: Biogeochemical processes at hydrothermal  
592 vents: microbes and minerals, bioenergetics, and carbon fluxes, *Oceanography*, 25, 196–208,  
593 <https://doi.org/http://dx.doi.org/10.5670/oceanog.2012.18>, 2012.

594 Homann, V. V., Sandy, M., Tincu, J. A., Templeton, A. S., Tebo, B. M., and Butler, A.: Loihichelins A - F ,  
595 a Suite of Amphiphilic Siderophores Produced by the Marine Bacterium *Halomonas* LOB-5, *J. Nat. Prod.*,  
596 72, 884–888, 2009.

597 Honeyman, B. D. and Santschi, P. H.: A Brownian-pumping model for oceanic trace metal scavenging:  
598 evidence from Th isotopes, 1989.

599 Kato, C. and Nogi, Y.: Correlation between phylogenetic structure and function : examples from deep-sea  
600 *Shewanella*, 35, 223–230, 2001.

601 Kelley, D. S. and Shank, T. M.: Hydrothermal systems: A decade of discovery in slow spreading  
602 environments, *Geophys. Monogr. Ser.*, 188, 369–407, <https://doi.org/10.1029/2010GM000945>, 2010.

603 Kleint, C., Hawkes, J. A., Sander, S. G., and Koschinsky, A.: Voltammetric Investigation of Hydrothermal  
604 Iron Speciation, *Front. Mar. Sci.*, 3, 1–11, <https://doi.org/10.3389/fmars.2016.00075>, 2016.

605 Kuhn, K. M., Maurice, P. A., States, U., Neubauer, E., Hofmann, T., and Kammer, F. Von Der: Accessibility  
606 of Humic-Associated Fe to a Microbial Siderophore: Implications for Bioavailability, *Environ. Sci. Technol.*,  
607 1015–1022, 2014.

608 Kumler, W. and Ingalls, A. E.: The R Journal: Tidy Data Neatly Resolves Mass-Spectrometry’s Ragged  
609 Arrays, *R J.*, 2022.

610 Laglera, L. M. and van den Berg, C. M. G.: Evidence for geochemical control of iron by humic substances  
611 in seawater, *Limnol. Oceanogr.*, 54, 610–619, 2009.

612 Lauderdale, J. M., Braakman, R., Forget, G., Dutkiewicz, S., and Follows, M. J.: Microbial feedbacks  
613 optimize ocean iron availability, *Proc. Natl. Acad. Sci. U. S. A.*, 117, 4842–4849,  
614 <https://doi.org/10.1073/pnas.1917277117>, 2020.

615 Li, M., Toner, B. M., Baker, B. J., Breier, J. a, Sheik, C. S., and Dick, G. J.: Microbial iron uptake as a  
616 mechanism for dispersing iron from deep-sea hydrothermal vents., *Nat. Commun.*, 5, 3192,  
617 <https://doi.org/10.1038/ncomms4192>, 2014.

618 Lough, A. J. M., Homoky, W. B., Connelly, D. P., Nakamura, K., Abyaneh, M. K., Kaulich, B., and Mills,  
619 R. A.: Soluble iron conservation and colloidal iron dynamics in a hydrothermal plume, *Chem. Geol.*,  
620 <https://doi.org/10.1016/j.chemgeo.2019.01.001>, 2019.

621 Lough, A. J. M., Tagliabue, A., Demasy, C., Resing, J. A., Mellett, T., Wyatt, N. J., and Lohan, M. C.: The  
622 impact of hydrothermal vent geochemistry on the addition of iron to the deep ocean, *Biogeosciences Discuss.*,  
623 [preprint], 1–23, <https://doi.org/10.5194/bg-2022-73>, 2022.

624 Mackey, D. J. and Zirino, A.: Comments on trace metal speciation in seawater or do “onions” grow in the  
625 sea?, *Anal. Chim. Acta*, 284, 635–647, 1994.

626 Mahieu, L., Whitby, H., Dulaquais, G., Tilliette, C., Guigue, C., Tedetti, M., Lefevre, D., Fourier, P.,  
627 Bressac, M., Sarthou, G., Bonnet, S., Guieu, C., and Salaün, P.: Iron-binding by dissolved organic matter in  
628 the Western Tropical South Pacific Ocean (GEOTRACES TONGA cruise GPP14), *Front. Mar. Sci.*, 11,  
629 <https://doi.org/10.3389/fmars.2024.1304118>, 2024.

630 Manck, L. E., Park, J., Tully, B. J., Poire, A. M., Bundy, R. M., Dupont, C. L., and Barbeau, K. A.:

631 Petrobactin, a siderophore produced by *Alteromonas*, mediates community iron acquisition in the global  
632 ocean, *ISME J.*, 16, 358–369, <https://doi.org/10.1038/s41396-021-01065-y>, 2022.

633 Martinez, J. S., Carter-Franklin, J. N., Mann, E. L., Martin, J. D., Haygood, M. G., and Butler, A.: Structure  
634 and membrane affinity of a suite of amphiphilic siderophores produced by a marine bacterium, *Proc. Natl.*  
635 *Acad. Sci. U. S. A.*, 100, 3754–3759, <https://doi.org/10.1073/pnas.0637444100>, 2003.

636 Mellett, T., Albers, J. B., Santoro, A., Wang, W., Salaun, P., Resing, J., Lough, A. J., Tagliabue, A., Lohan,  
637 M., Bundy, R. M., and Buck, K. N.: Particle exchange mediated by organic ligands in incubation experiments  
638 of hydrothermal vent plumes along the mid-Atlantic Ridge, n.d.

639 Misumi, K., Lindsay, K., Moore, J. K., Doney, S. C., Tsumune, D., and Yoshida, Y.: Humic substances may  
640 control dissolved iron distributions in the global ocean: Implications from numerical simulations, *Global*  
641 *Biogeochem. Cycles*, 27, 450–462, 2013.

642 Moore, L. E., Heller, M. I., Barbeau, K. A., Moffett, J. W., and Bundy, R. M.: Organic complexation of iron  
643 by strong ligands and siderophores in the eastern tropical North Pacific oxygen deficient zone, *Mar. Chem.*,  
644 236, 104021, <https://doi.org/10.1016/j.marchem.2021.104021>, 2021.

645 Muller, F. L. L.: Exploring the Potential Role of Terrestrially Derived Humic Substances in the Marine  
646 Biogeochemistry of Iron, *Front. Earth Sci.*, 6, 1–20, <https://doi.org/10.3389/feart.2018.00159>, 2018.

647 Omanović, D., Gamier, C., and Pižeta, I.: ProMCC: An all-in-one tool for trace metal complexation studies,  
648 *Mar. Chem.*, 173, 25–39, <https://doi.org/10.1016/j.marchem.2014.10.011>, 2015.

649 Parada, A. E., Needham, D. M., and Fuhrman, J. A.: Every base matters: Assessing small subunit rRNA  
650 primers for marine microbiomes with mock communities, time series and global field samples, *Environ.*  
651 *Microbiol.*, 18, 1403–1414, <https://doi.org/10.1111/1462-2920.13023>, 2016.

652 Park, J., Durham, B. P., Key, R. S., Groussman, R. D., Pinedo-Gonzalez, P., Hawco, N. J., John, S. G.,  
653 Carlson, M. C. G., Lindell, D., Juraneck, L., Ferrón, S., Ribalet, F., Armbrust, E. V., Ingalls, A. E., and Bundy,  
654 R. M.: Siderophore production and utilization by microbes in the North Pacific Ocean, *bioRxiv*,  
655 2022.02.26.482025, <https://doi.org/10.1101/2022.02.26.482025>, 2022.

656 Park, J., Durham, B. P., Key, R. S., Groussman, R. D., Bartolek, Z., Pinedo-Gonzalez, P., Hawco, N. J., John,  
657 S. G., Carlson, M. C. G., and Lindell, D.: Siderophore production and utilization by marine bacteria in the  
658 North Pacific Ocean, *Limnol. Oceanogr.*, 68, 1636–1653, 2023.

659 Quast, C., Pruesse, E., Yilmaz, P., Gerken, J., Schweer, T., Yarza, P., Peplies, J., and Glöckner, F. O.: The  
660 SILVA ribosomal RNA gene database project: Improved data processing and web-based tools, *Nucleic Acids*  
661 *Res.*, 41, 590–596, <https://doi.org/10.1093/nar/gks1219>, 2013.

662 Reitz, Z. L., Butler, A., and Medema, M. H.: Automated genome mining predicts combinatorial diversity and  
663 taxonomic distribution of peptide metallophore structures, *bioRxiv*, 15–20,  
664 <https://doi.org/https://doi.org/10.1101/2022.12.14.519525>, 2022.

665 Resing, J. a., Sedwick, P. N., German, C. R., Jenkins, W. J., Moffett, J. W., Sohst, B. M., and Tagliabue, A.:  
666 Basin-scale transport of hydrothermal dissolved metals across the South Pacific Ocean, *Nature*, 523, 200–  
667 203, <https://doi.org/10.1038/nature14577>, 2015.

668 Rizzi, A., Roy, S., Bellenger, J. P., and Beaugard, P. B.: Iron homeostasis in *Bacillus subtilis* requires  
669 siderophore production and biofilm formation, *Appl. Environ. Microbiol.*, 85,  
670 <https://doi.org/10.1128/AEM.02439-18>, 2019.

671 Ruttkies, C., Schymanski, E. L., Wolf, S., Hollender, J., and Neumann, S.: MetFrag relaunched: incorporating  
672 strategies beyond in silico fragmentation, *J. Cheminform.*, 8, 1–16, [https://doi.org/10.1186/s13321-016-](https://doi.org/10.1186/s13321-016-0115-9)  
673 0115-9, 2016.

674 Sander, S. G. and Koschinsky, A.: Metal flux from hydrothermal vents increased by organic complexation,  
675 *Nat. Geosci.*, 4, 145–150, <https://doi.org/10.1038/ngeo1088>, 2011.

676 Sandy, M. and Butler, A.: Microbial iron acquisition: marine and terrestrial siderophores., *Chem. Rev.*, 109,  
677 4580–95, <https://doi.org/10.1021/cr9002787>, 2009.

678 Santoro, A. E., Casciotti, K. L., and Francis, C. A.: Activity, abundance and diversity of nitrifying archaea  
679 and bacteria in the central California Current, *Environ. Microbiol.*, 12, 1989–2006,  
680 <https://doi.org/10.1111/j.1462-2920.2010.02205.x>, 2010.

681 Sheik, C. S., Anantharaman, K., Breier, J. A., Sylvan, J. B., Edwards, K. J., and Dick, G. J.: Spatially resolved  
682 sampling reveals dynamic microbial communities in rising hydrothermal plumes across a back-arc basin.,  
683 *ISME J.*, 9, 1434–45, <https://doi.org/10.1038/ismej.2014.228>, 2015.

684 Slatger, H. A., Laglera, L. M., Sukekava, C., and Gerringa, L. J. A.: Fe-Binding Organic Ligands in the  
685 Humic-Rich TransPolar Drift in the Surface Arctic Ocean Using Multiple Voltammetric Methods, *J.*  
686 *Geophys. Res. Ocean.*, 124, 1491–1508, <https://doi.org/10.1029/2018JC014576>, 2019.

687 Sorokina, M., Merseburger, P., Rajan, K., Yirik, M. A., and Steinbeck, C.: COCONUT online: Collection of  
688 Open Natural Products database, *J. Cheminform.*, 13, 1–13, <https://doi.org/10.1186/s13321-020-00478-9>,  
689 2021.

690 Stephens, B. M., Opalk, K., Petras, D., Liu, S., Comstock, J., Aluwihare, L. I., Hansell, D. A., and Carlson,  
691 C. A.: Organic Matter Composition at Ocean Station Papa Affects Its Bioavailability, Bacterioplankton  
692 Growth Efficiency and the Responding Taxa, *Front. Mar. Sci.*, 7, <https://doi.org/10.3389/fmars.2020.590273>,  
693 2020.

694 Sumner, L. W., Amberg, A., Barrett, D., Beale, M. H., Beger, R., Daykin, C. A., Fan, T. W.-M., Fiehn, O.,  
695 Goodacre, R., Griffin, J. L., Hankemeier, T., Hardy, N., Hamly, J., Higashi, R., Kopka, J., Lane, A. N.,  
696 Lindon, J. C., Marriott, P., Nicholls, A. W., Reily, M. D., Thaden, J. J., and Viant, M. R.: Proposed minimum  
697 reporting standards for chemical analysis, *Metabolomics*, 3, 211–221, <https://doi.org/10.1007/s11306-007-0082-2>, 2007.

699 Tagliabue, A., Bowie, A. R., Boyd, P. W., Buck, K. N., Johnson, K. S., and Saito, M. A.: The integral role  
700 of iron in ocean biogeochemistry, *Nature*, 543, 51–59, <https://doi.org/10.1038/nature21058>, 2017.

701 Toner, B. M., Fakra, S. C., Manganini, S. J., Santelli, C. M., Marcus, M. a., Moffett, J. W., Rouxel, O.,  
702 German, C. R., and Edwards, K. J.: Preservation of iron(II) by carbon-rich matrices in a hydrothermal plume,  
703 *Nat. Geosci.*, 2, 197–201, <https://doi.org/10.1038/ngeo433>, 2009.

704 Tortell, P. D., Maldonado, M. T., and Price, N. M.: The role of heterotrophic bacteria in iron-limited ocean  
705 ecosystems, *Nature*, 383, 330–332, <https://doi.org/10.1038/383330a0>, 1996.

706 Vraspir, J. M. and Butler, A.: Chemistry of marine ligands and siderophores., *Ann. Rev. Mar. Sci.*, 1, 43–63,  
707 <https://doi.org/10.1146/annurev.marine.010908.163712>, 2009.

708 Wang, H., Wang, W., Liu, M., Zhou, H., Ellwood, M. J., Butterfield, D. A., Buck, N. J., and Resing, J. A.:  
709 Iron ligands and isotopes in hydrothermal plumes over backarc volcanoes in the Northeast Lau Basin,  
710 Southwest Pacific Ocean, *Geochim. Cosmochim. Acta*, 336, 341–352, 2022.

711 Waska, H., Koschinsky, A., Ruiz Chanco, M. J., and Dittmar, T.: Investigating the potential of solid-phase  
712 extraction and Fourier-transform ion cyclotron resonance mass spectrometry (FT-ICR-MS) for the isolation  
713 and identification of dissolved metal-organic complexes from natural waters, *Mar. Chem.*, 173, 78–92,  
714 <https://doi.org/10.1016/j.marchem.2014.10.001>, 2015.

715 Whitby, H., Planquette, H., Cassar, N., Bucciarelli, E., Osburn, C. L., Janssen, D. J., Cullen, J. T., González,  
716 A. G., Völker, C., and Sarthou, G.: A call for refining the role of humic-like substances in the oceanic iron  
717 cycle, *Sci. Rep.*, 10, 6144, 2020.

718 Whitby, H., Park, J., Shaked, Y., Boiteau, R. M., Buck, K. N., and Bundy, R. M.: New insights into the  
719 organic complexation of bioactive trace metals in the global ocean from the GEOTRACES era,  
720 *Oceanography*, 37, 142–155, 2024.

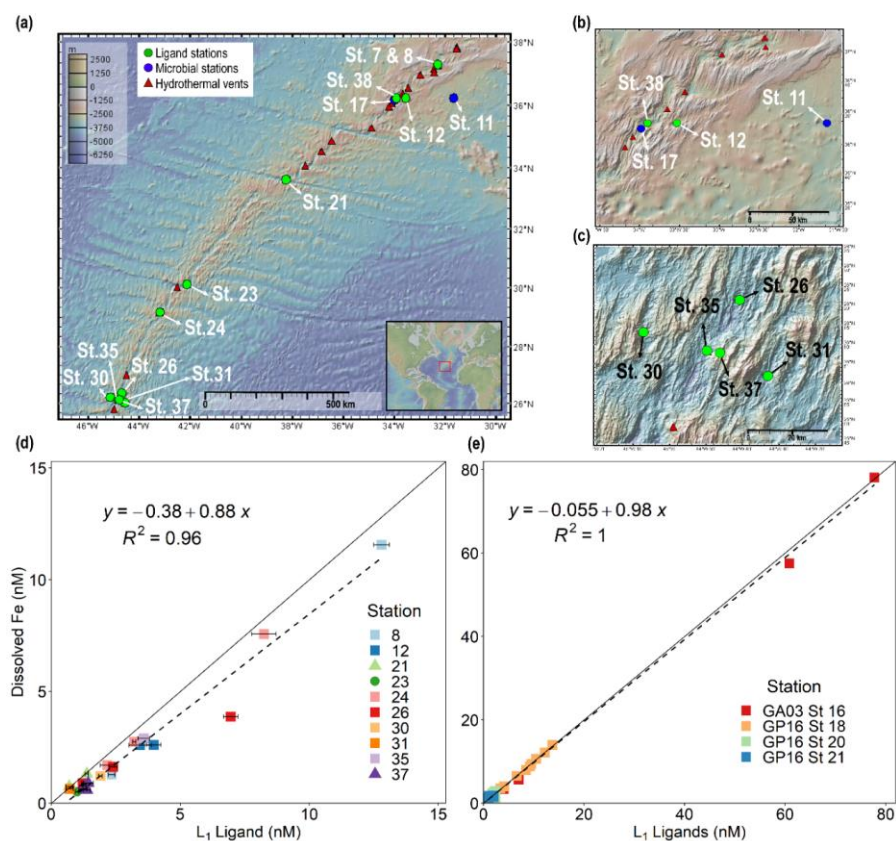
721 Yücel, M., Gartman, A., Chan, C. S., and Luther, G. W.: Hydrothermal vents as a kinetically stable source  
722 of iron-sulphide-bearing nanoparticles to the ocean, *Nat. Geosci.*, 4, 367–371,  
723 <https://doi.org/10.1038/ngeo1148>, 2011.

724 .

725

726 **Figures and Tables**

727



728

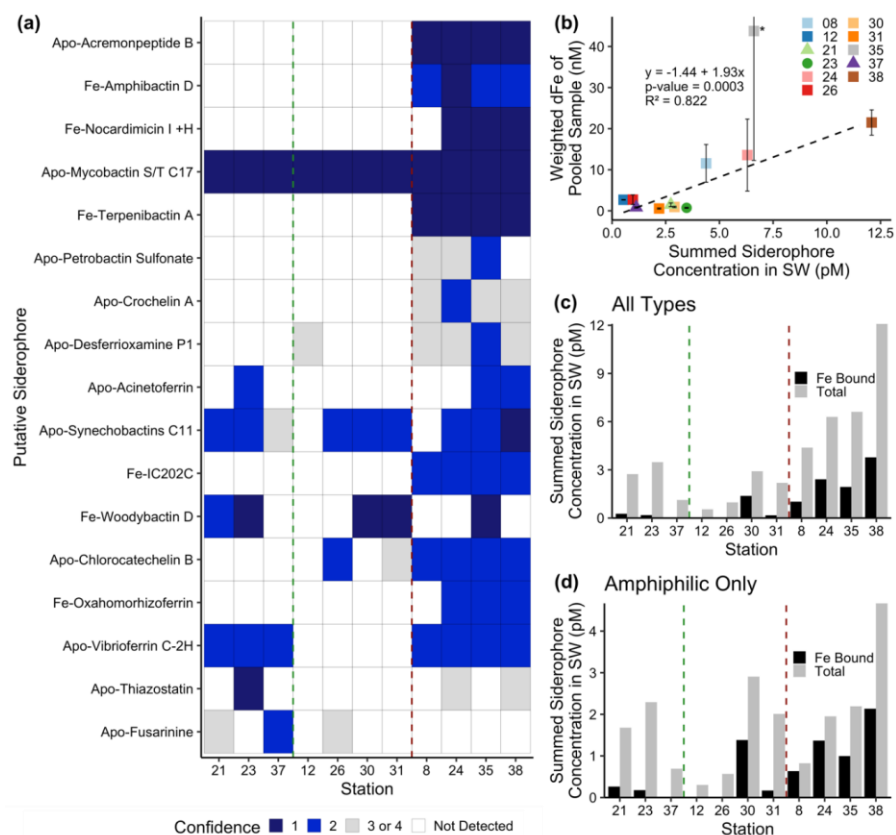
729 **Figure 1. Dissolved iron is strongly correlated with L<sub>1</sub> iron-binding ligands in diverse hydrothermal**

730 **systems.** (a) Station map showing the 11 sites investigated along the MAR. Known hydrothermal vents are

731 marked as red triangles (Beaulieu and Szafranski, 2020). Two expanded inset maps for (b) Rainbow and (c)

732 TAG hydrothermal vent fields. For additional information about vent site characteristics refer to **Table 1.** (d)

733 dFe versus  $L_1$  iron-binding ligands at each vent site in this study showing a ~1:1 correlation ( $m=0.88$ ,  $R^2=$   
734  $0.96$ ) with dFe in neutrally-buoyant plumes along the MAR. (e) dFe versus  $L_1$  ligands from previous studies  
735 over the ridge axis and ~80 km from ridge axis in the Southern East Pacific Rise hydrothermal plume (Buck  
736 et al., 2018), and over TAG hydrothermal vent field (Buck et al., 2015). The solid black lines in (d) and (e)  
737 are the 1:1 ratio line between dFe and ligand concentrations, and dashed lines show the linear regression for  
738 the corresponding data. Square symbols refer to spreading centers, triangles refer to fracture zones, and  
739 circles refer to alkaline vents. Error bars represent the 95% confidence interval of the data fit as calculated  
740 by ProMCC (Omanović et al., 2015). The map was created using GeoMapApp version 3.6.14.  
741  
742



743

744

745 **Figure 2. Siderophore presence in hydrothermal plumes along the MAR.** (a) Heat map of confidence  
 746 levels 1-2 (blue gradient, 1 = highest confidence). Gray boxes indicate a detection with lower confidence (see  
 747 Methods), and white boxes indicate no detection at those sites. The y-axis is ordered from top to bottom in  
 748 terms of descending mass of the apo (without Fe) form of the siderophore. (b) Model III ordinary least squares  
 749 regression on dFe versus summed siderophore concentrations (of detections in Fig. 2b), calculated from peak  
 750 areas, at each site. Since the siderophore analysis was performed on pooled samples, the dFe values in the  
 751 regression are weighted values based on measured dFe and volume of each constituent of the pooled sample.  
 752 The vertical error bars represent the standard deviation of dFe of the constituents. TAG (St. 35) — denoted  
 753 by the asterisk — was not included in the regression due to its large range of dFe values and outlier behavior.  
 754 (c-d) Fe bound versus total summed concentration of (c) all types of siderophores and (d) amphiphilic  
 755 siderophores at each station. The vertical green lines separate fracture/diffuse sites from off-axis sites and  
 756 vertical red lines separate off-axis from on-axis sites as defined in Table 1. Symbols follow Fig. 1.

757



758

759

760 **Figure 3. Relative abundance of putative siderophore-producing taxa.** Bar height indicates the proportion  
 761 of 16S rRNA genes recovered in each sample, separated by depth from water surface, filter size fraction, and  
 762 site location. Colors correspond to taxonomy. Genera found in MAR vent microbial communities with  
 763 members in the antimash database predicted to produce siderophores are depicted at the family level.

764

Table 1. Characteristics of sample locations along the Mid Atlantic Ridge.

Vent Names	Abbr.	Station	Geology	Host rock	Vent type	Spreading rate (mm/yr)	Summed putative siderophore concentration (pM)	Summed Siderophore concentration/ L <sub>1</sub> ligand (%)*
Lucky Strike	LS	7/8	Spreading Center	gabbro	Black smoker	20.2	4.38	0.034-0.19
33 km E of Rainbow	CER	12	Spreading Center	-	-	-	0.537	0.013-0.017
Rainbow	R	38	Spreading Center	ultramafic	Black smoker	20.6	12.1	<i>n.a.</i>
Hayes Fracture Zone	HFZ	21	Fracture Zone	peridotites/gabbro	-	21.2	2.74	0.20-0.39
Lost City	LC	23	Fracture Zone	ultramafic/gabbro	Alkaline	22.6	3.47	0.27-0.35
Broken Spur	BS	24	Spreading Center	gabbro	Black smoker/diffuse	22.9	6.30	0.07-0.29
29 km N of TAG	CNT	26	Spreading Center	-	-	-	0.968	0.014-0.079
30 km W of TAG	CWT	30	Spreading Center	-	-	-	2.91	0.15
30 km E of TAG	CET	31	Spreading Center	-	-	-	2.19	0.31



Trans-Atlantic Geotraverse	TAG	35	Spreading Center	gabbro	Black smoker	23.6	6.61	0.18
Low Temp Slope	LTS	37	-	-	Diffuse fluids	-	1.13	0.079-0.087

Spreading rates along the Mid-Atlantic Ridge were gathered from the Interridge Database v3.4. Host rock groups were determined from previously discussed classifications (Bazylev, 1997; Kelley and Shank, 2010). Off-axis sites –33 km E of Rainbow, 29 km N of TAG, 30 km E of TAG, and 30 km W of TAG– were far-field locations of their respective vent field. Low Temp Slope was a diffuse-dominated site that was sampled for the first time as a part of this study. Summed putative siderophore concentrations and the percent of L<sub>1</sub> ligand are reported for compounds detected with at least confidence level 1 and 2 at one site. These values do not take into account typical extraction efficiencies of ENV columns for Fe-binding organics. Average L<sub>1</sub> ligand and siderophore concentrations can be viewed in **Table S3** and concentrations for individual siderophores can be observed in **Table S5**.

\*The siderophore sample at each site was pooled from ligand samples, so the percentage of siderophores in the L<sub>1</sub> pool is presented as a range based on the range of L<sub>1</sub> concentrations at each site.

*n.a.* = unable to be determined

- = unknown

